ACS Photonics

pubs.acs.org/journal/apchd5

Article

Frequency Tripling via Sum-Frequency Generation at the Nanoscale

Attilio Zilli, Davide Rocco, Marco Finazzi,* Agostino Di Francescantonio, Lamberto Duò, Carlo Gigli, Giuseppe Marino, Giuseppe Leo, Costantino De Angelis, and Michele Celebrano

Cite This: *ACS Photonics* 2021, 8, 1175–1182

Read Online

ACCESS | Metrics & More | Article Recommendations | Supporting Information

ABSTRACT: High refractive index dielectric nanostructures can be exploited to enhance nonlinear optical processes via the strong light confinement by their resonant modes. The sensitive dependence of these modes on the geometry and material composition offers ample opportunities for tailoring the optical response of the system. Here we report sum-frequency generation (SFG) by individual AlGaAs nanocylinders, pumped by two pulsed beams at a telecommunication frequency, ω, and its duplicate, 2ω. Under such a scheme, the SFG at $3\omega = \omega + 2\omega$ is degenerate with the third-harmonic generation (THG) seeded by the input at ω, thereby tripling its frequency via the second-order permittivity $\chi^{(2)}$, rather than via $\chi^{(3)}$ as in THG. The concurrent detection of THG and SFG enables us to determine $\chi^{(3)} = 7 \times 10^{-20}$ m^2/V^2 by comparing experiments to numerical simulations and based on the known value of $\chi^{(2)}$. We observe a rich size- and polarization-dependent behavior that gives appeal to the studied system as a key component of miniaturized photonic devices.

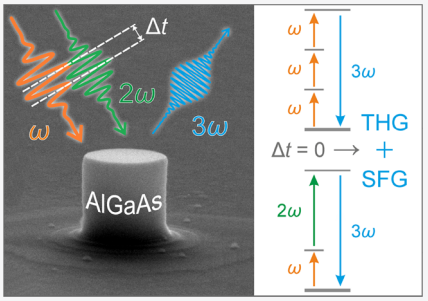

KEYWORDS: *nonlinear nanophotonics, III−V nanoantennas, aluminum gallium arsenide, sum-frequency generation, third-harmonic generation, anapole*

Multiple electromagnetic waves can interact in a material through nonlinear optical processes to generate coherent light of a different frequency. The ability to realize and harness such processes at the nanoscale paves the way to new functionalities in compact photonic devices. Nonetheless, the small volume of matter involved means that the efficiency attained in nonlinear conversion is typically poor. The electromagnetic resonances of nanostructures can be exploited to boost the efficiency, first by confining and enhancing the fields within small volumes, and second by coupling effectively the localized fields to the exciting and emitted waves traveling in free space.[1] To such an aim, the resonances of the system, and their coherent interference, can be engineered to a large extent by tuning the geometry and material composition of the structure.[2]

Although metal nanostructures were explored first for this purpose,[3] dielectric-based nanophotonics has gained much traction in recent years.[4,5] Transparency in the visible and near-infrared spectral ranges represents the key advantage of dielectric nano-objects, which enables them to withstand more intense radiant fluxes and sustain resonances with a higher quality factor in comparison to metal nano-objects, whose response is governed by Ohmic losses. Moreover, unlike their metal counterparts, high-index dielectric nano-objects can sustain strong magnetic resonances and high-order Mie-type modes in the visible and near-infrared range.[2,6,7] These resonances underpin a strong nonlinear response, thanks to their large modal volume located inside the bulk of the material,[8,9] in contrast to metals where the resonant fields are tightly confined at the surface.

Semiconductor materials hold much promise for technological applications, as they rely on a mature fabrication technology and are easily integrated into miniaturized optical circuitry. Semiconductors of group IV (Si, Ge) can exhibit a large third-order susceptibility $\chi^{(3)}$. Indeed, resonant enhancement and control of third-harmonic generation (THG)[10−17] as well as of other nondegenerate four-wave mixing processes[18,19] have been reported at the level of a single nano-object or multimer. Conversely, semiconductor compounds and alloys of the groups III−V often exhibit a large second-order susceptibility $\chi^{(2)}$ because of the lack of inversion symmetry of their crystal lattice. Indeed, efficient second-harmonic generation (SHG) has been observed in single nanoantennas of GaP[20] and GaAs.[21−23] Among III−Vs, monolithic AlGaAs antennas have emerged as a performing platform for nanoscale nonlinear optics, demonstrating efficient SHG,[24−30] THG,[30] and precise control of the directionality of the nonlinear emission;[31,32] furthermore, the possibility of exploiting the high quality factor associated with bound states in the

Received: January 20, 2021
Published: March 12, 2021

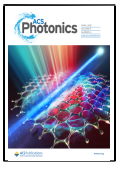

https://dx.doi.org/10.1021/acsphotonics.1c00112
ACS Photonics 2021, 8, 1175−1182

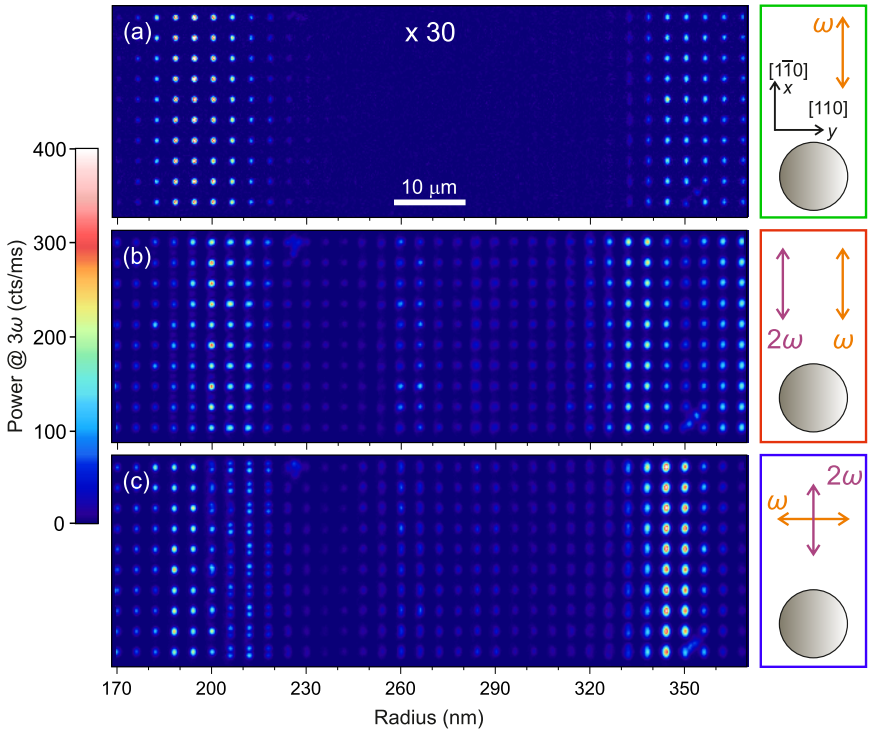

Figure 1. Epi-detected confocal raster scans of the cylinder array where the power detected at 3ω is encoded in false colors. The sketches on the right of each map represent the frequency and polarization of the pump(s) employed: a pulsed beam at ω alone (a) or superimposed to a pulsed beam at 2ω either co- (b) or cross- (c) polarized to it. The pump powers are given in the text. The crystalline axes of AlGaAs are oriented as indicated in the top-right sketch.

continuum was recently highlighted.[33,34] Notably, these antennas are amenable to enhancing second-order processes other than SHG, such as the optical parametric generation of entangled photon pairs.[35] In this Article we report the experimental observation of sum-frequency generation (SFG), whereby two pulses at a telecommunication frequency and the duplicate frequency interact coherently in a single nanoantenna to generate visible light at the THG frequency.

OPTICAL MEASUREMENTS

The investigated sample contains $Al_{0.18}Ga_{0.82}As$ cylinders of 400 nm height and radius R ranging between 165 and 365 nm, with their axis oriented along the [001] crystal direction. The resonators, obtained by electron-beam lithography, are supported by a low-refractive index (n = 1.6) AlOx substrate, resulting in a strong optical confinement within the AlGaAs volume (n = 3.2). The fabrication protocol[24] is reported in Section S.I of the Supporting Information (SI), along with some electron microscopy characterization of the sample.

The same Section S.I includes a detailed description of our nonlinear microscope. Briefly, our laser source emits pulses of τ = 160 fs duration at a repetition rate of ν = 80 MHz, centered at an angular frequency ω corresponding to the wavelength λ = 1554 nm. This beam is partially duplicated in frequency (to $\lambda/2$ = 777 nm) via a beta barium borate (BBO) crystal. The beams at ω and 2ω are recombined and focused onto the sample via a 0.85 numerical aperture (NA) air microscope objective. The temporal delay between the two pulse trains is controlled by a delay line in the ω beam path. The nonlinear emission is collected through the same objective in a backscattering configuration (see Figure S2) and optically filtered to a narrow band around $\lambda/3$ = 518 nm. The emitted power is measured using a single-photon avalanche diode, whose small sensor (50 μm diameter) acts as a pinhole, implementing a confocal detection scheme whereby out-of-focus light (generated in the substrate) is rejected.

Figure 1 presents exemplary confocal maps detected at 3ω by raster-scanning the sample under the laser beam via a piezoelectric microscope stage. The individual cylinders, arranged in a square array of 3 μm pitch, appear as well-resolved bright spots. R increases in steps of 6 nm along the y direction, whereas along the x direction one has 10 nominally identical replicas. Map a is excited solely by pulses at ω, whereas maps b and c are concurrently excited by pulses at ω and 2ω, which are spatially and temporally superimposed on the sample, and either co- (b) or cross- (c) polarized. The sample was illuminated with a time-averaged power of $P_{avg}(\omega)$ = 384 μW and $P_{avg}(2\omega)$ = 192 μW, corresponding (based on a diffraction-limited spot assumption) to an instantaneous (pulse peak) intensity of $I_{pk}(\omega)$ = 1.15 GW/cm^2 and $I_{pk}(2\omega)$ = 2.30 GW/cm^2. Comparing maps b and c with a, one sees that the additional input at 2ω brings about an increase in the nonlinear emission at 3ω by over an order of magnitude. In all three maps, two resonant geometries occur at about R = 200 and 345 nm. Interestingly, the latter resonance exhibits a marked dependence on the relative polarization of the two pumps, whereby a local minimum is observed for co-polarized excitation (map b) in correspondence to a maximum for cross-polarized excitation (map c). Conversely, the resonance at R = 200 nm is excited regardless of the pump polarizations. The observed radial dependence is underpinned by a magnetic dipole (MD) mode (with a sizable electric dipole contribution)[24] and an anapole (AP),[36] which are tuned to ω respectively for R = 200 and 345 nm; see Section S.II of the SI. The response is further modulated by the spatial

https://dx.doi.org/10.1021/acsphotonics.1c00112
ACS Photonics 2021, 8, 1175−1182

overlap of the fields with higher-order multipolar modes resonating at 2ω.[24,28]

A first-order AP is a resonant field distribution whereby a toroidal dipole and an electric dipole mode oscillate coherently in antiphase. Due to the destructive interference of the two radiation patterns in the far-field, this configuration corresponds to a minimum of the scattering cross-section and thus, owing to the low radiative losses, to a maximum of the internal energy.[37,38] APs therefore can be exploited to boost the nonlinear conversion efficiency, as recently reported for THG[12,13] and SHG.[21] Lastly, we emphasize that the achievement of such zero-scattering condition does not violate Lorentz reciprocity theorem as APs are not eigenmodes of the open cavity: they can be excited by external radiation, and indeed cannot self-sustain in its absence.[39]

We report in Figure 2 some pieces of experimental evidence, which support our hypothesis that the nonlinear emission observed in Figure 1b,c is SFG at $3\omega = \omega + 2\omega$. The emission spectra of single cylinders having R within the MD and AP resonance ranges are displayed in panels a and b, respectively. These data were acquired with an imaging spectrometer equipped with a charge-coupled device (CCD) camera, see details in Section S.I of the SI. The spectra exhibit single peaks centered at 518 nm (corresponding to $\lambda/3$) with no discernible multiphoton luminescence background over a broad spectral range, thereby also confirming the pure THG character of the emission excited at ω. The fwhm of all peaks ranges between 4 and 5 nm, in comparison to the 17 nm fwhm of the laser pulse at ω. Finally, it should be noted that excitation at 2ω alone brings about no detectable signal across the whole wavelength range detected (not shown).

Incidentally, let us note that the THG emission contains a contribution of the cascaded frequency-tripling pathway ($\omega + \omega \rightarrow 2\omega$, followed by $\omega + 2\omega \rightarrow 3\omega$), whose yield can be comparable to the direct pathway ($\omega + \omega + \omega \rightarrow 3\omega$) in nanostructures with large second-order nonlinearities.[40] It is hard, however, to tell apart the two processes experimentally, because they emit at the same frequency, share the same (cubic) power dependence and even the same symmetry properties (i.e., same polarization response) in a crystal of the cubic family such as AlGaAs.

Figure 2c,d display the dependence of the power emitted at 3ω (the portion generated by the interaction of ω and 2ω) on the instantaneous (pulse peak) intensity of one pump, while the other one is kept fixed. The linear dependence on either pump intensity observed for both MD and AP resonances, and for both co- and cross-polarized excitation, is a distinctive signature of SFG.

By varying the delay between the ω and 2ω pulses, we studied their nonlinear mixing in the time domain and recorded traces such as those shown in Figure 2e,f, which are measured on single cylinders having R within the MD (e) and AP (f) ranges. All traces exhibit intense and symmetric temporal correlation peaks emerging from a flat THG baseline generated by the ω beam alone. Such results indicate a nonlinear interaction mediated by fast ($\lesssim$100 fs) electronic processes rather than by a photothermal mechanism, which instead would bring about asymmetric traces with much longer (~10 ps) phonon thermalization tails. Specifically, assuming an instantaneous interaction, the delay trace can be modeled analytically as the intensity correlation between a Gaussian pulse at ω and its squared and time-delayed replica at 2ω. Based on the nominal pulse duration of 160 fs, the fwhm of the analytical delay curve is 194 fs. The comparison with the measured fwhm values of about 390 fs suggest that both pump pulses are sizably stretched in duration, which is consistent with the several cm of glass included in the excitation path. The delay traces we recorded do not exhibit interference between SFG and THG, although both are emitted coherently at 3ω, because the latter is comparatively weak for the chosen pump powers and, more generally, because their interference is prevented by the symmetry arguments presented in Section S.IV of the SI.

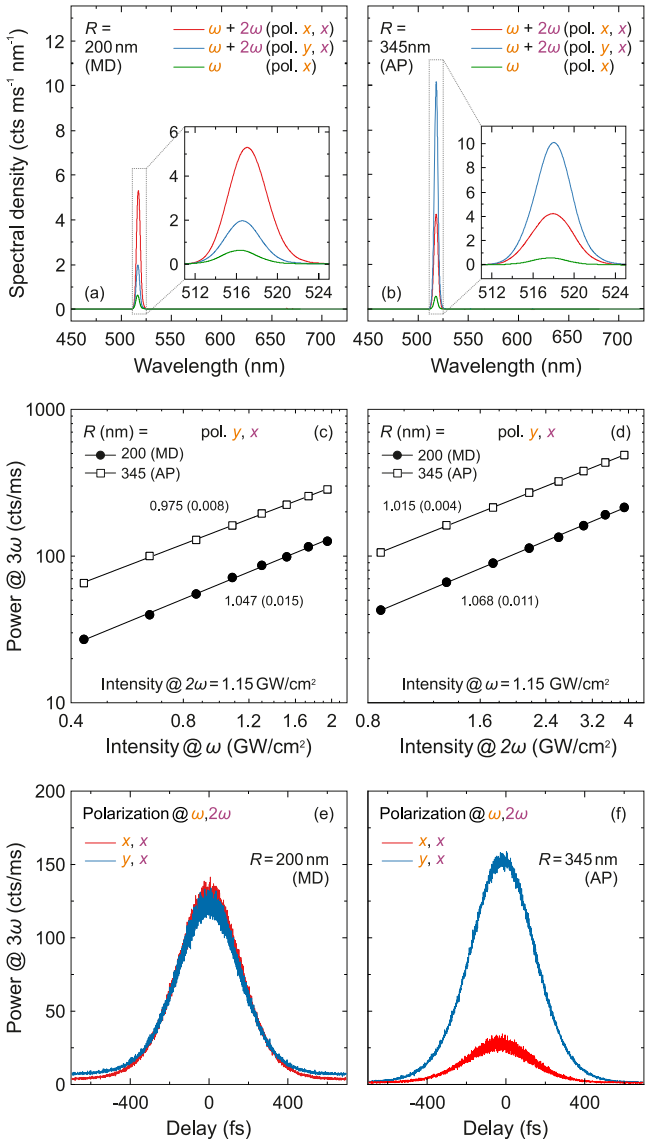

Figure 2. (a, b) Emission spectra of a single cylinder of radius (a) R = 200 or (b) 345 nm. The pumps have polarization as indicated by the legends and intensity $I_{pk}(\omega)$ = 0.97 GW/cm^2 for x polarization and $I_{pk}(\omega)$ = 0.61 GW/cm^2 for y polarization; $I_{pk}(2\omega)$ = 1.1 GW/cm^2. (c, d) Dependence of the nonlinear emission of a single cylinder on the intensity of either pump, for different values of R indicated by the legends. The dots are the signal generated by the interaction of ω and 2ω, that is, after subtracting the THG contribution due to ω alone. The lines are power fits of the form $P(3\omega) \propto [I_{pk}(\omega,2\omega)]^p$. The fitting values of the power p are reported beside each line, with the uncertainty in brackets. (e, f) Delay traces recorded on a single cylinder having (e) R = 200 or (f) 345 nm. The pumps have polarization as indicated by the legends and intensity $I_{pk}(\omega)$ = 0.79 GW/cm^2 and $I_{pk}(2\omega)$ = 1.6 GW/cm^2.

https://dx.doi.org/10.1021/acsphotonics.1c00112
ACS Photonics 2021, 8, 1175−1182

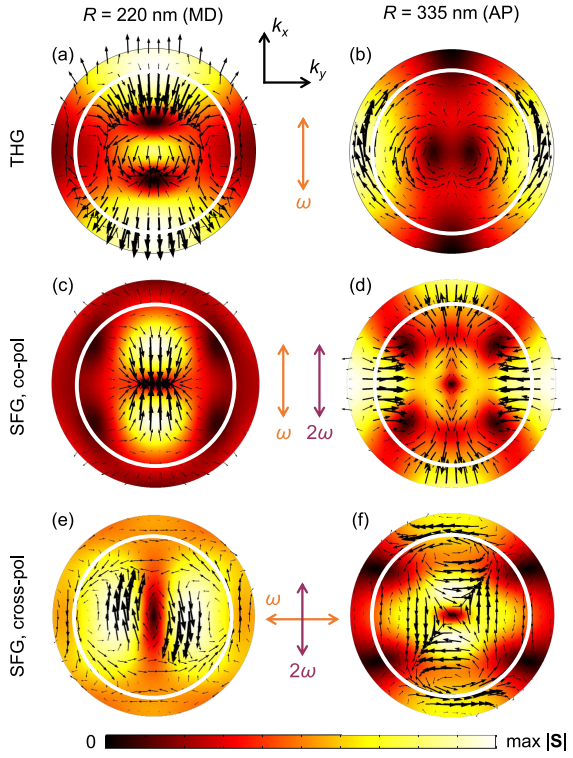

Figure 3. Simulated back-focal-plane images of the (a, b) THG or (c–f) SFG emission toward the air side of a single pillar of radius (a, c, e) R = 220 or (b, d, f) 335 nm. The polarization of the pumps is indicated by the double arrows in the middle of each image row. The electric fields $\mathbf{E}^{THG}$ and $\mathbf{E}^{SFG}$ are represented as arrow fields, and the magnitude of the Poynting vectors $\mathbf{S}^{THG}$ and $\mathbf{S}^{SFG}$ (proportional to $|\mathbf{E}^{THG}|^2$ and $|\mathbf{E}^{SFG}|^2$, respectively) is represented in false colors. The inner white circles mark the experimental collection range determined by the objective NA of 0.85.

NUMERICAL SIMULATIONS

Numerical simulations were performed to further validate our THG and SFG attributions, as well as to study the nature of the resonances involved and investigate the directionality of the nonlinear emission. In our model, a resonator is described as a cylinder of variable radius R and 400 nm height made of $Al_{0.18}Ga_{0.82}As$, whose wavelength-dependent permittivity is taken from ref 41. The cylinder lies on a flat AlOx substrate (refractive index n = 1.6) and is surrounded by air (n = 1.0). A commercial solver (COMSOL Multiphysics) was employed to solve numerically the electromagnetic wave equation in the frequency domain. We simulate the nonlinear response through two sequential computations. In the first one, performed at the fundamental wavelength ω and (for SFG simulations only) at 2ω, an external excitation is introduced in the form of a plane wave propagating perpendicularly to the substrate from the air side and linearly polarized along the [110] or [1$\bar{1}$0] crystal axis as in the experiment. This approximated description of the tightly focused illumination employed in experiments, which contains a sizable portion of longitudinal polarization, reduces substantially the computation times. We checked the effect of including non-normal wavevectors in the illumination in Figure S6c of the SI. The electric field, $\mathbf{E}$, computed at ω (and at 2ω too for SFG) induces a nonlinear polarization density $\mathbf{P}^{THG}$ (or $\mathbf{P}^{SFG}$) at 3ω. In a material with zincblende lattice ($F\bar{4}3m$ crystallographic space group) such as AlGaAs, one has

$$P_i^{THG}(3\omega) = \varepsilon_0 \left[\chi^{(3)}_{iiii} E_i^3(\omega) + 3\chi^{(3)}_{iijj} E_i(\omega) E_j^2(\omega) + 3\chi^{(3)}_{iikk} E_i(\omega) E_k^2(\omega)\right] \quad (1)$$

where $i \neq j \neq k$ indicate the Cartesian components x, y, and z. We tentatively assign to all nonzero components of the $\chi^{(3)}$ tensor the value of 10^{-19} m^2/V^2, reported for GaAs by ref 42. $\mathbf{P}^{SFG}$ is given by

$$P_i^{SFG}(3\omega) = \varepsilon_0 \chi^{(2)}_{ijk} \left[E_j(\omega) E_k(2\omega) + E_k(\omega) E_j(2\omega)\right] \quad (2)$$

with $i \neq j \neq k$. Following ref 24, we set all components of the $\chi^{(2)}$ tensor equal to 2×10^{-10} m/V.

Either $\mathbf{P}^{THG}$ or $\mathbf{P}^{SFG}$ is the source term of the wave equation in the second computation at 3ω. The computed local fields are projected to the far field toward the air side via the postprocessing tools offered by COMSOL (Stratton–Chu formula). The directional information in the far field is displayed in Figure 3 in the form of back-focal-plane images for a resonator having R in the MD (images on the left) or AP (images on the right) resonance range. The arrow fields represent $\mathbf{E}^{THG}$ and $\mathbf{E}^{SFG}$. Their symmetries under rotation and mirroring can be predicted based on the symmetry of the pump fields and of the crystal lattice, see Section S.IV of the SI. In particular, $\mathbf{E}^{THG}$ and $\mathbf{E}^{SFG}$ always have opposite parity with respect to one coordinate plane; consequently, their interference (given by the integral of their product over the detection range indicated by the white circles) is null, as anticipated above. The magnitude of the Poynting vectors $\mathbf{S}^{THG}$ and $\mathbf{S}^{SFG}$, proportional to the emitted power density, is represented in false colors. The patterns have the 2-fold rotational symmetry of both the illumination and the zincblende lattice seen along the [001] direction. Note that the SFG at the AP condition under co-polarized excitation (image d) is emitted largely outside of the detection range of the objective, whereas for cross-polarized pumps (image f), the emission occurs mostly at small values of the wavevector components $k_{x,y}$. Conversely, for the MD mode (images c and e), the emission is collected almost completely regardless of the pump polarizations. These remarks explain in part the different behaviors at the MD and AP resonances under co- and cross-polarized excitation that we observed in Figure 1b,c.

RESULTS AND DISCUSSION

We used the numerical model described above for investigating the effect of the geometry of the resonator on the nonlinear signal and, particularly, the dependence on R. The measured nonlinear signals are modeled as the flux of $\mathbf{S}(3\omega)$ within the solid angle corresponding to the experimental detection. The simulated THG and SFG signals are reported in Figure 4b,d side-by-side to the corresponding measurements in panels a and c. The experimental data points are the values of the most intense pixel in the confocal image of the cylinder. To reduce the uncertainty due the dispersity of the sample, we mediated over the 10 nominally identical cylinders along the x direction. To reduce the systematic errors due to possible asymmetries of the illumination or of the sample, we mediated over two orthogonal and, in principle, equivalent orientations of the sample; see the discussion in Section S.V of the SI, where the two data sets being averaged are reported.

By comparing the measured and simulated data, to the left and right side of Figure 4, respectively, an overall agreement is found, with the following noteworthy discrepancies. To start with, the peak positions are slightly different, most markedly

https://dx.doi.org/10.1021/acsphotonics.1c00112
ACS Photonics 2021, 8, 1175–1182

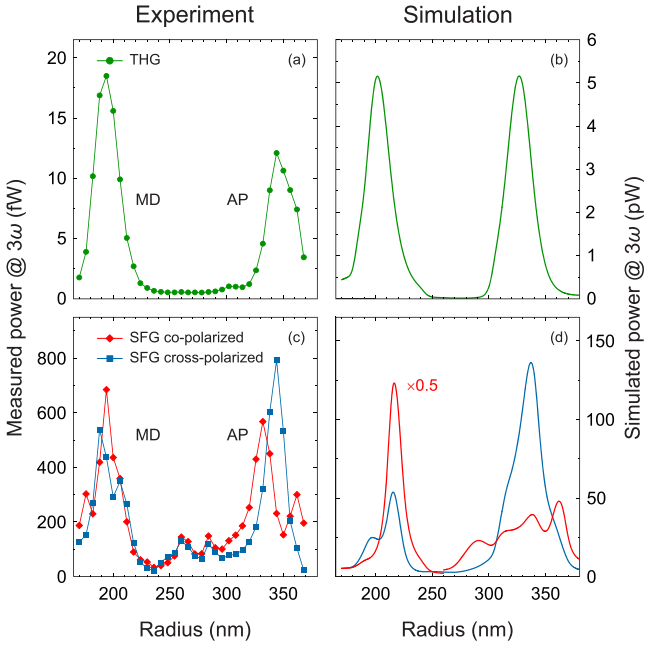

Figure 4. (a, b) THG and (c, d) SFG time-averaged power emitted by a single cylinder as a function of its radius. For both measured (a, c) and simulated (b, d) data, the pump powers are $P_{avg}(\omega) = 384\ \mu W$ and $P_{avg}(2\omega) = 192\ \mu W$. The experimental data points are the most intense pixel value averaged over 10 nominally identical cylinders and 2 theoretically equivalent orthogonal sample orientations (see text).

for the MD peaks, which occur at about 190 nm in the experiment and 210 nm in the simulation. Second, in terms of relative amplitudes, the two resonances are very close in the THG simulations, whereas in the experiment the emission at the AP is weaker. As for SFG, the effect of the pump polarization is greater in the simulations, most notably with the co-polarized MD peak being about 5× more intense than its co-polarized counterpart, which is not the case in the experimental data. Generally speaking, we ascribe the discrepancies listed above to differences between the model cylinders and the measured ones, in terms of geometry (inclination of the axis[27] and overall shape) and material composition (e.g., crystalline orientation and surface contamination). We therefore studied the dependence of the simulated SFG emission as a function of R on the cylinder height (Figure S6a) and on the in-plane sample orientation (Figure S6b). Interestingly, we found out that an in-plane rotation (in either direction) of the crystalline axes brings closer the co- and cross-polarized MD peak amplitudes, see the detailed discussion in Section S.VI. Indeed, one sees stronger co-to-cross-polarization dynamics in Figure S5c,d than in Figure 4c, where the contrast is washed out by averaging.

Let us now turn our attention to comparing the absolute peak magnitudes. It is in the first place apparent that the simulated power is a few hundred times higher than the measured one: this can be due to losses in the detection path beyond the nominal efficiency of the optical elements, which are already accounted for in the quantification of the experimental power. It is, however, more instructive to look at the SFG-to-THG power ratio, which is about 600 fW/15 fW = 40 in the experiment and 100 pW/5 pW = 20 in the simulation. While we reckon that the experimental ratio is quite solid, as SFG and THG are detected concurrently and at the same frequency, the simulated powers, on the other hand, are respectively proportional to $\left|\chi^{(2)}\right|^2$ and $\left|\chi^{(3)}\right|^2$, which are not precisely known; especially the latter one, for which we used the reported GaAs value[42] of $\chi^{(3)} = 10^{-19}\ m^2/V^2$ as an educated guess. To match the experimental ratio, one should then reduce $\chi^{(3)}$ by a factor $\sqrt{40/20} = 1.4$, which gives $\chi^{(3)} = 7 \times 10^{-20}\ m^2/V^2$. Let us emphasize that we could have used in our simulations any *ansatz* value other than $\chi^{(3)} = 10^{-19}\ m^2/V^2$, so that the value of $\chi^{(3)}$ we determined is based solely on the established literature value[24] of $\chi^{(3)} = 2 \times 10^{-10}$ m/V. Admittedly, this procedure is affected by large systematics (for instance, because the simulated powers of the nonlinear emission depend on the instantaneous pump intensity, which is retrieved from the measured powers through assumptions on the spatial and temporal profile of the excitation), and the resulting value of $\chi^{(3)}$, therefore, should be regarded as an order-of-magnitude estimate. Nonetheless, it is worth considering that relatively few materials have been characterized in terms of $\chi^{(3)}$, and that often independent reports on the same material differ by a few orders of magnitude. To summarize, on one hand we have found a $\chi^{(3)}$ of AlGaAs in line (within the estimated uncertainty) with GaAs; on the other hand, we have illustrated a procedure that can be applied to other nanostructured nonlinear materials and potentially with higher accuracy.

Let us now assess the experimental efficiency of THG and SFG based on the powers emitted at resonance reported in Figure 4a and c, respectively. In order to have a metric independent from the characteristics (time-averaged power P_{avg}, pulse duration $\tau = 160$ fs, and pulse repetition rate $\nu = 80$ MHz) of our input beams, a nonlinear coefficient γ is customarily defined in terms of the instantaneous (pulse peak) powers, $P_{pk} = P_{avg}/(\tau\nu)$, as

$$\gamma^{THG} \equiv \frac{P_{pk}^{THG}(3\omega)}{P_{pk}^{3}(\omega)} = 5.2 \times 10^{-14}\ W^{-2} \tag{3a}$$

$$\gamma^{SFG} \equiv \frac{P_{pk}^{SFG}(3\omega)}{P_{pk}(\omega)P_{pk}(2\omega)} = 1.2 \times 10^{-10}\ W^{-1} \tag{3b}$$

By inserting an analyzer in the detection path, we characterized the polarization of the nonlinear emission at 3ω by a single cylinder with R in the range corresponding to the MD resonance and the AP condition. The results are reported in the left column of Figure 5. Since the geometry of the cylinder is axially symmetric and the pumps are always oriented along the equivalent [110] or [1$\bar{1}$0] crystal axes, all polarization plots exhibit the 2-fold symmetry of the excitation. While the THG is always oriented parallel to the exciting polarization at ω, the SFG exhibits a more varied behavior as a function of R: for instance, under co-polarized excitation it is parallel to both pumps at the MD and perpendicular to both pumps at the AP. The measurements display some asymmetry of the lobes and a discrepancy in the power after a 360° rotation of the polarization, which we attribute to the mechanical drift of the sample stage or the pump superposition over the acquisition time (approximately 30 min per plot). The corresponding simulated data are reported on the right column of Figure 5. While some differences are visible—most markedly the broader lobes of the simulated THG—the overall agreement to experiment is good, thereby further

https://dx.doi.org/10.1021/acsphotonics.1c00112
ACS Photonics 2021, 8, 1175−1182

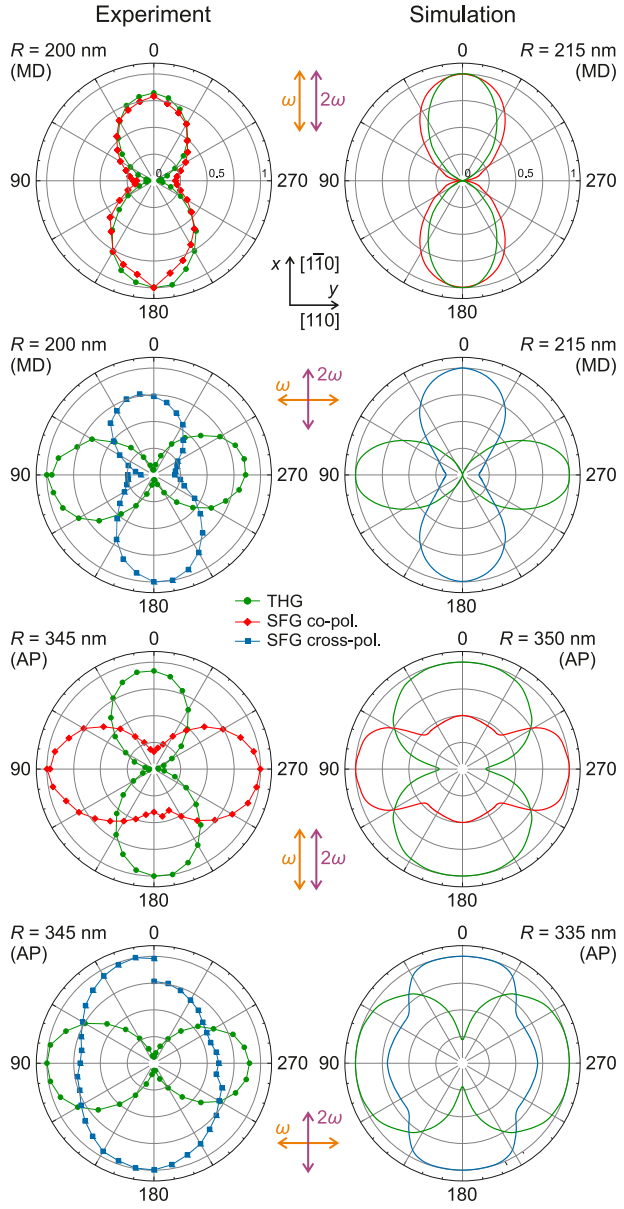

Figure 5. Measured (left) and simulated (right) normalized power emitted at 3ω by a single cylinder as a function of the detected polarization angle. The arrows in the middle indicate the pump polarizations used for the plots on both their sides. The sample orientation is the same as Figures 1 and 3.

confirming the THG and SFG characters of the observed nonlinear signals.

CONCLUSIONS

In conclusion, we demonstrated SFG in individual $Al_{0.18}Ga_{0.82}As$ resonators. Such nonlinear mixing can be used to upconvert and redirect a coherent signal at the nanoscale. The frequency-degenerate SFG scheme we implemented offers an efficient $\chi^{(2)}$-based frequency-tripling pathway alternative to THG. The concurrent measurement of the frequency-degenerate SFG and THG allowed us to estimate the ratio $\chi^{(2)}/\chi^{(3)}$ by comparison to numerical simulations. Such an estimate is valuable considering the scarcity of $\chi^{(3)}$ measurements in literature—to the best of our knowledge, we have reported here for the first time the $\chi^{(3)}$ of AlGaAs—and inasmuch as our method can be applied to other nanoresonators made of a different material. Finally, the sensitive dependence of the nonlinear emission on the excitation (pump polarizations) and on the geometry of the system (cylinder radius) makes the studied system promising as the constituting element of a nonlinear reconfigurable metasurface, where one beam is used as a control to perform all-optical information encoding[43] or logic operation.

ASSOCIATED CONTENT

Supporting Information

The Supporting Information is available free of charge at https://pubs.acs.org/doi/10.1021/acsphotonics.1c00112.

S.I: Materials and methods; S.II: Character of the electromagnetic resonances; S.III: Simulated emission toward the substrate; S.IV: Symmetry and interference of the THG and SFG fields; S.V: Systematics related to the orientation of the sample; S.VI: Dependence of the numerical model on some parameters (PDF)

AUTHOR INFORMATION

Corresponding Author

Marco Finazzi − *Politecnico di Milano, Physics Department, 20133 Milano, Italy;* orcid.org/0000-0002-9197-3654; Email: marco.finazzi@polimi.it

Authors

Attilio Zilli − *Politecnico di Milano, Physics Department, 20133 Milano, Italy;* orcid.org/0000-0003-1845-6850

Davide Rocco − *Università di Brescia, Department of Information Engineering, 25123 Brescia, Italy*

Agostino Di Francescantonio − *Politecnico di Milano, Physics Department, 20133 Milano, Italy;* orcid.org/0000-0002-7987-5349

Lamberto Duò − *Politecnico di Milano, Physics Department, 20133 Milano, Italy*

Carlo Gigli − *Université de Paris, Physics Department, 75013 Paris, France;* orcid.org/0000-0001-8327-0425

Giuseppe Marino − *Université de Paris, Physics Department, 75013 Paris, France;* orcid.org/0000-0001-8979-051X

Giuseppe Leo − *Université de Paris, Physics Department, 75013 Paris, France;* orcid.org/0000-0001-6525-6734

Costantino De Angelis − *Università di Brescia, Department of Information Engineering, 25123 Brescia, Italy;* orcid.org/0000-0001-8029-179X

Michele Celebrano − *Politecnico di Milano, Physics Department, 20133 Milano, Italy;* orcid.org/0000-0003-3336-3580

Complete contact information is available at: https://pubs.acs.org/10.1021/acsphotonics.1c00112

Notes

The authors declare no competing financial interest.

ACKNOWLEDGMENTS

A.Z., D.R., C.D.A., and M.C. acknowledge financial support by the Italian Ministry of Education, University and Research (MIUR) through the PRIN project "NOMEN" (2017MP7F8F). G.L. acknowledges financial support by the French National Research Agency (ANR) through the project NANOPAIR (ANR-18-CE92-0043). All authors thank Aristide Lemaître for the epitaxial growth of the sample.

REFERENCES

(1) De Angelis, C., Leo, G., Neshev, D. N., Eds. *Nonlinear Meta-Optics*; CRC Press, 2020, DOI: 10.1201/b22515.
(2) Smirnova, D.; Kivshar, Y. S. Multipolar nonlinear nanophotonics. *Optica* **2016**, *3*, 1241−1255.
(3) Kauranen, M.; Zayats, A. V. Nonlinear plasmonics. *Nat. Photonics* **2012**, *6*, 737−748.
(4) Kuznetsov, A. I.; Miroshnichenko, A. E.; Brongersma, M. L.; Kivshar, Y. S.; Luk'yanchuk, B. Optically resonant dielectric nanostructures. *Science* **2016**, *354*, aag2472.
(5) Koshelev, K.; Kivshar, Y. Dielectric resonant metaphotonics. *ACS Photonics* **2021**, *8*, 102−112.
(6) Evlyukhin, A. B.; Novikov, S. M.; Zywietz, U.; Eriksen, R. L.; Reinhardt, C.; Bozhevolnyi, S. I.; Chichkov, B. N. Demonstration of magnetic dipole resonances of dielectric nanospheres in the visible region. *Nano Lett.* **2012**, *12*, 3749−3755.
(7) Kuznetsov, A. I.; Miroshnichenko, A. E.; Fu, Y. H.; Zhang, J.; Luk'yanchuk, B. Magnetic light. *Sci. Rep.* **2012**, *2*, 492.
(8) Smirnova, D. A.; Khanikaev, A. B.; Smirnov, L. A.; Kivshar, Y. S. Multipolar third-harmonic generation driven by optically induced magnetic resonances. *ACS Photonics* **2016**, *3*, 1468−1476.
(9) Smirnova, D.; Smirnov, A. I.; Kivshar, Y. S. Multipolar second-harmonic generation by Mie-resonant dielectric nanoparticles. *Phys. Rev. A* **2018**, *97*, 013807.
(10) Shcherbakov, M. R.; Neshev, D. N.; Hopkins, B.; Shorokhov, A. S.; Staude, I.; Melik-Gaykazyan, E. V.; Decker, M.; Ezhov, A. A.; Miroshnichenko, A. E.; Brener, I.; Fedyanin, A. A.; Kivshar, Y. S. Enhanced third-harmonic generation in silicon nanoparticles driven by magnetic response. *Nano Lett.* **2014**, *14*, 6488−6492.
(11) Shorokhov, A. S.; Melik-Gaykazyan, E. V.; Smirnova, D. A.; Hopkins, B.; Chong, K. E.; Choi, D.-Y.; Shcherbakov, M. R.; Miroshnichenko, A. E.; Neshev, D. N.; Fedyanin, A. A.; Kivshar, Y. S. Multifold enhancement of third-harmonic generation in dielectric nanoparticles driven by magnetic Fano resonances. *Nano Lett.* **2016**, *16*, 4857−4861.
(12) Grinblat, G.; Li, Y.; Nielsen, M. P.; Oulton, R. F.; Maier, S. A. Enhanced third harmonic generation in single germanium nanodisks excited at the anapole mode. *Nano Lett.* **2016**, *16*, 4635−4640.
(13) Grinblat, G.; Li, Y.; Nielsen, M. P.; Oulton, R. F.; Maier, S. A. Efficient third harmonic generation and nonlinear subwavelength imaging at a higher-order anapole mode in a single germanium nanodisk. *ACS Nano* **2017**, *11*, 953−960.
(14) Melik-Gaykazyan, E. V.; Shcherbakov, M. R.; Shorokhov, A. S.; Staude, I.; Brener, I.; Neshev, D. N.; Kivshar, Y. S.; Fedyanin, A. A. Third-harmonic generation from Mie-type resonances of isolated all-dielectric nanoparticles. *Philos. Trans. R. Soc. A* **2017**, *375*, 20160281.
(15) Wang, L.; Kruk, S.; Xu, L.; Rahmani, M.; Smirnova, D.; Solntsev, A.; Kravchenko, I.; Neshev, D.; Kivshar, Y. Shaping the third-harmonic radiation from silicon nanodimers. *Nanoscale* **2017**, *9*, 2201−2206.
(16) Melik-Gaykazyan, E. V.; Kruk, S. S.; Camacho-Morales, R.; Xu, L.; Rahmani, M.; Zangeneh Kamali, K.; Lamprianidis, A.; Miroshnichenko, A. E.; Fedyanin, A. A.; Neshev, D. N.; Kivshar, Y. S. Selective third-harmonic generation by structured light in Mie-resonant nanoparticles. *ACS Photonics* **2018**, *5*, 728−733.
(17) Xu, L.; Rahmani, M.; Zangeneh Kamali, K.; Lamprianidis, A.; Ghirardini, L.; Sautter, J.; Camacho-Morales, R.; Chen, H.; Parry, M.; Staude, I.; Zhang, G.; Neshev, D.; Miroshnichenko, A. E. Boosting third-harmonic generation by a mirror-enhanced anapole resonator. *Light: Sci. Appl.* **2018**, *7*, 44.
(18) Grinblat, G.; Li, Y.; Nielsen, M. P.; Oulton, R. F.; Maier, S. A. Degenerate four-wave mixing in a multiresonant germanium nanodisk. *ACS Photonics* **2017**, *4*, 2144−2149.
(19) Colom, R.; Xu, L.; Marini, L.; Bedu, F.; Ozerov, I.; Begou, T.; Lumeau, J.; Miroshnishenko, A. E.; Neshev, D.; Kuhlmey, B. T.; Palomba, S.; Bonod, N. Enhanced four-wave mixing in doubly resonant Si nanoresonators. *ACS Photonics* **2019**, *6*, 1295−1301.
(20) Sanatinia, R.; Anand, S.; Swillo, M. Modal engineering of second-harmonic generation in single GaP nanopillars. *Nano Lett.* **2014**, *14*, 5376−5381.
(21) Timofeeva, M.; Lang, L.; Timpu, F.; Renaut, C.; Bouravleuv, A.; Shtrom, I.; Cirlin, G.; Grange, R. Anapoles in free-standing III−V nanodisks enhancing second-harmonic generation. *Nano Lett.* **2018**, *18*, 3695−3702.
(22) Sautter, J. D.; Xu, L.; Miroshnichenko, A. E.; Lysevych, M.; Volkovskaya, I.; Smirnova, D. A.; Camacho-Morales, R.; Zangeneh Kamali, K.; Karouta, F.; Vora, K.; Tan, H. H.; Kauranen, M.; Staude, I.; Jagadish, C.; Neshev, D. N.; Rahmani, M. Tailoring second-harmonic emission from (111)-GaAs nanoantennas. *Nano Lett.* **2019**, *19*, 3905−3911.
(23) Xu, L.; Saerens, G.; Timofeeva, M.; Smirnova, D. A.; Volkovskaya, I.; Lysevych, M.; Camacho-Morales, R.; Cai, M.; Zangeneh Kamali, K.; Huang, L.; Karouta, F.; Tan, H. H.; Jagadish, C.; Miroshnichenko, A. E.; Grange, R.; Neshev, D. N.; Rahmani, M. Forward and backward switching of nonlinear unidirectional emission from GaAs nanoantennas. *ACS Nano* **2020**, *14*, 1379−1389.
(24) Gili, V. F.; Carletti, L.; Locatelli, A.; Rocco, D.; Finazzi, M.; Ghirardini, L.; Favero, I.; Gomez, C.; Lemaître, A.; Celebrano, M.; De Angelis, C.; Leo, G. Monolithic AlGaAs second-harmonic nanoantennas. *Opt. Express* **2016**, *24*, 15965−15971.
(25) Camacho-Morales, R.; Rahmani, M.; Kruk, S.; Wang, L.; Xu, L.; Smirnova, D. A.; Solntsev, A. S.; Miroshnichenko, A.; Tan, H. H.; Karouta, F.; Naureen, S.; Vora, K.; Carletti, L.; De Angelis, C.; Jagadish, C.; Kivshar, Y. S.; Neshev, D. N. Nonlinear generation of vector beams from AlGaAs nanoantennas. *Nano Lett.* **2016**, *16*, 7191−7197.
(26) Kruk, S. S.; Camacho-Morales, R.; Xu, L.; Rahmani, M.; Smirnova, D. A.; Wang, L.; Tan, H. H.; Jagadish, C.; Neshev, D. N.; Kivshar, Y. S. Nonlinear optical magnetism revealed by second-harmonic generation in nanoantennas. *Nano Lett.* **2017**, *17*, 3914−3918.
(27) Gili, V. F.; Carletti, L.; Chouchane, F.; Wang, G.; Ricolleau, C.; Rocco, D.; Lemaître, A.; Favero, I.; Ghirardini, L.; Finazzi, M.; Celebrano, M.; De Angelis, C.; Leo, G. Role of the substrate in monolithic AlGaAs nonlinear nanoantennas. *Nanophotonics* **2017**, *7*, 517−521.
(28) Ghirardini, L.; Carletti, L. F.; Gili, V.; Pellegrini, G.; Duò, L.; Finazzi, M.; Rocco, D.; Locatelli, A.; De Angelis, C.; Favero, I.; Ravaro, M.; Leo, G.; Lemaître, A.; Celebrano, M. Polarization properties of second-harmonic generation in AlGaAs optical nanoantennas. *Opt. Lett.* **2017**, *42*, 559−562.
(29) Carletti, L.; Rocco, D.; Locatelli, A.; De Angelis, C.; Gili, V. F.; Ravaro, M.; Favero, I.; Leo, G.; Finazzi, M.; Ghirardini, L.; Celebrano, M.; Marino, G.; Zayats, A. V. Controlling second-harmonic generation at the nanoscale with monolithic AlGaAs-on-AlOx antennas. *Nanotechnology* **2017**, *28*, 114005.
(30) Camacho-Morales, R.; Bautista, G.; Zang, X.; Xu, L.; Turquet, L.; Miroshnichenko, A.; Tan, H. H.; Lamprianidis, A.; Rahmani, M.; Jagadish, C.; Neshev, D. N.; Kauranen, M. Resonant harmonic generation in AlGaAs nanoantennas probed by cylindrical vector beams. *Nanoscale* **2019**, *11*, 1745−1753.
(31) Ghirardini, L.; Marino, G.; Gili, V. F.; Favero, I.; Rocco, D.; Carletti, L.; Locatelli, A.; De Angelis, C.; Finazzi, M.; Celebrano, M.; Neshev, D. N.; Leo, G. Shaping the nonlinear emission pattern of a dielectric nanoantenna by integrated holographic gratings. *Nano Lett.* **2018**, *18*, 6750−6755.
(32) Carletti, L.; Marino, G.; Ghirardini, L.; Gili, V. F.; Rocco, D.; Favero, I.; Locatelli, A.; Zayats, A. V.; Celebrano, M.; Finazzi, M.; Leo, G.; De Angelis, C.; Neshev, D. N. Nonlinear goniometry by second-harmonic generation in AlGaAs nanoantennas. *ACS Photonics* **2018**, *5*, 4386−4392.
(33) Carletti, L.; Koshelev, K.; De Angelis, C.; Kivshar, Y. Giant nonlinear response at the nanoscale driven by bound states in the continuum. *Phys. Rev. Lett.* **2018**, *121*, 033903.

https://dx.doi.org/10.1021/acsphotonics.1c00112
ACS Photonics 2021, 8, 1175−1182

(34) Koshelev, K.; Kruk, S.; Melik-Gaykazyan, E.; Choi, J.-H.; Bogdanov, A.; Park, H.-G.; Kivshar, Y. Subwavelength dielectric resonators for nonlinear nanophotonics. *Science* **2020**, *367*, 288−292.
(35) Marino, G.; Solntsev, A. S.; Xu, L.; Gili, V. F.; Carletti, L.; Poddubny, A. N.; Rahmani, M.; Smirnova, D. A.; Chen, H.; Lemaître, A.; Zhang, G.; Zayats, A. V.; De Angelis, C.; Leo, G.; Sukhorukov, A. A.; Neshev, D. N. Spontaneous photon-pair generation from a dielectric nanoantenna. *Optica* **2019**, *6*, 1416−1422.
(36) Rocco, D.; Gili, V. F.; Ghirardini, L.; Carletti, L.; Favero, I.; Locatelli, A.; Marino, G.; Neshev, D. N.; Celebrano, M.; Finazzi, M.; Leo, G.; De Angelis, C. Tuning the second-harmonic generation in AlGaAs nanodimers via non-radiative state optimization. *Photonics Res.* **2018**, *6*, B6−B12.
(37) Miroshnichenko, A. E.; Evlyukhin, A. B.; Yu, Y. F.; Bakker, R. M.; Chipouline, A.; Kuznetsov, A. I.; Luk'yanchuk, B.; Chichkov, B. N.; Kivshar, Y. S. Nonradiating anapole modes in dielectric nanoparticles. *Nat. Commun.* **2015**, *6*, 8069.
(38) Yang, Y.; Bozhevolnyi, S. I Nonradiating anapole states in nanophotonics: from fundamentals to applications. *Nanotechnology* **2019**, *30*, 204001.
(39) Monticone, F.; Sounas, D.; Krasnok, A.; Alu, A. Can a nonradiating mode be externally excited? Nonscattering states versus embedded eigenstates. *ACS Photonics* **2019**, *6*, 3108−3114.
(40) Celebrano, M.; Locatelli, A.; Ghirardini, L.; Pellegrini, G.; Biagioni, P.; Zilli, A.; Wu, X.; Grossmann, S.; Carletti, L.; De Angelis, C.; Duo, L.; Hecht, B.; Finazzi, M. Evidence of cascaded third-harmonic generation in noncentrosymmetric gold nanoantennas. *Nano Lett.* **2019**, *19*, 7013−7020.
(41) Gehrsitz, S.; Reinhart, K. F.; Gourgon, C.; Herres, N.; Vonlanthen, A.; Sigg, H. The refractive index of $Al_xGa_{1-x}As$ below the band gap: Accurate determination and empirical modeling. *J. Appl. Phys.* **2000**, *87*, 7825−7837.
(42) Vincenti, M. A.; de Ceglia, D.; Roppo, V.; Scalora, M. Harmonic generation in metallic, GaAs-filled nanocavities in the enhanced transmission regime at visible and UV wavelengths. *Opt. Express* **2011**, *19*, 2064−2078.
(43) Myers, C. J.; Celebrano, M.; Krishnan, M. Information storage and retrieval in a single levitating colloidal particle. *Nat. Nanotechnol.* **2015**, *10*, 886−891.

NOTE ADDED AFTER ASAP PUBLICATION

This paper was published ASAP on March 12, 2021, with errors in equations 2, 3a, and 3b and Figure 4. The corrected version of equations 3a and 3b and Figure 4 was reposted on March 15, 2021. The corrected version of equation 2 was reposted on March 16, 2021.

https://dx.doi.org/10.1021/acsphotonics.1c00112
ACS Photonics 2021, 8, 1175−1182